Journal of Power Sources 196 (2011) 4655–4670

Contents lists available at ScienceDirect

Journal of Power Sources

journal homepage: www.elsevier.com/locate/jpowsour

Analysis and control of a fuel delivery system considering a two-phase anode model of the polymer electrolyte membrane fuel cell stack

Jinglin He*, Jongwoo Ahn[1], Song-Yul Choe[2]

Department of Mechanical Engineering, Auburn University, Auburn, AL 36832, USA

ARTICLE INFO

Article history:
Received 15 September 2010
Received in revised form 2 January 2011
Accepted 7 January 2011
Available online 18 January 2011

Keywords:
PEM fuel cell
Control
Two-phase
Ejector

ABSTRACT

The fuel delivery system using both an ejector and a blower for a PEM fuel cell stack is introduced as a fuel efficiency configuration because of the possibility of hydrogen recirculation dependent upon load states.

A high pressure difference between the cathode and anode could potentially damage the thin polymer electrolyte membrane. Therefore, the hydrogen pressure imposed to the stack should follow any change of the cathode pressure. In addition, stoichiometric ratio of the hydrogen should be maintained at a constant to prevent a fuel starvation at abrupt load changes.

Furthermore, liquid water in the anode gas flow channels should be purged out in time to prevent flooding in the channels and other layers. The purging control also reduces the impurities concentration in cells to improve the cell performance.

We developed a set of control oriented dynamic models that include a anode model considering the two-phase phenomenon and system components The model is used to design and optimize a state feedback controller along with an observer that controls the fuel pressure and stoichiometric ratio, whereby purging processes are also considered. Finally, included is static and dynamic analysis with respect to tracking and rejection performance of the proposed control.

© 2011 Elsevier B.V. All rights reserved.

1. Introduction

The polymer electrolyte membrane (PEM) fuel cell is widely considered as one of the best candidates to replace the internal combustion engine (ICE) in the future because of its relatively high efficiency, high power density, near to zero emissions, low working temperature, and short start-up time. For the vehicle application, additional subsystems such as the air supply system, fuel delivery system, and water and thermal management systems, must be designed to regulate the operating conditions of the fuel cell stacks under different load requests.

In these additional subsystems known as balance-of-plant (BOP), the fuel delivery system (FDS) supplies the hydrogen from a high-pressure tank, purges the impurities and liquid water in fuel cells, and reuses the hydrogen existing from the stack by way of a recirculation loop. FDS should supply sufficient hydrogen to the anode of the fuel cell stack to prevent any shortage of hydrogen that frequently happens at the dynamic current request from the vehicle. In addition, the pressure of hydrogen at anodic side should follow the air pressure at the cathode side, since the large pressure difference between them can potentially lead to a damage of the thin membranes in fuel cells.

Moreover, the water is transported from cathode side and may be condensed in anode gas flow channels, which causes flooding and blocks channels. The impurities of the hydrogen lead to contamination of catalysts. Both these excessive liquid water and impurities in the anodic side should be removed by periodic purging to prevent decrease of fuel cell performance. Thus, controls of the fuel flow rate, pressure and purging under a rapidly varying current request are three important objectives that should be considered in the FDS.

Review of recent publications shows that a few articles have discussed the FDS and the associated controls. Most researchers modeled the FDS as a part of the whole fuel cell system. The model of the FDS proposed by Pukrushpan et al. [1] was used to design controls using a flow control valve and purging valve without a recirculation design. Bao et al. [2] used an ejector in the FDS as a recirculation pump, but the recirculation flow rate was not actively controlled. Karnik et al. [3] built a FDS model that considered one supply line and one ejector recirculation line to improve water

* Corresponding author. Tel.: +1 3344448789; fax: +1 3348443307.
E-mail addresses: hejingl@auburn.edu (J. He), ahnjong@auburn.edu (J. Ahn), choe@eng.auburn.edu (S.-Y. Choe).
[1] Tel.: +1 3345594676; fax: +1 3348443307.
[2] Tel.: +1 3343298787; fax: +1 3348443307.

0378-7753/$ – see front matter © 2011 Elsevier B.V. All rights reserved.
doi:10.1016/j.jpowsour.2011.01.019

Nomenclature

a_w	water activity
A	area (m^2)
C	gas concentration ($kg\,m^{-3}$)
D	diameter (m) or diffusion coefficient ($m^2\,s^{-1}$)
F	Faraday constant (96,487 $C\,mol^{-1}$)
h_l	liquid water transfer coefficient
h_m	mass transfer coefficient ($m\,s^{-1}$)
I_{den}	current density ($A\,cm^{-2}$)
J	rotational inertia ($kg\,m^2$)
j	flux ($kg\,m^{-2}\,s^{-1}$)
m	mass (kg)
M	Mach number
N_{cell}	cell number
p	pressure (Pa, or bar)
Q	volume flux (SLPM)
R	gas constant ($J\,kg^{-1}\,K^{-1}$)
s	liquid saturation
S	reduced liquid saturation
T	temperature (K)
t	time (s)
U	velocity ($m\,s^{-1}$)
V	volume (m^3)
W	mass flow rate ($kg\,s^{-1}$)
y	mass fraction
γ	specific heat ratio
δ	thickness (m)
ε	porosity
η	efficiency
λ	water content
μ	viscosity ($kg\,s^{-1}\,m^{-1}$)
ρ	mass density ($kg\,m^{-3}$)
ω	angular velocity ($rad\,s^{-1}$)
τ	torque (Nm)

Subscripts

an	anode
bl	blower
bm	blower motor
ca	cathode
cl	catalyst layer
ej	ejector
em	ejector manifold
fcv	flow control valve
g	mixed gas
gfc	gas flow channel
gdl	gas diffusion layer
i	index of gas species
lpr	low-pressure regulator
max	maximum value
p	primary
pem	membrane
purge	purge valve
ref	reference
rm	return manifold
s	secondary
sat	saturation
sm	supply manifold
v	vapor
w	water

management in the fuel cell, where a flow control valve was used to supply hydrogen flow. However, three control objectives aforementioned could not be simultaneously met by using only one actuator. He et al. [4] proposed a controller for a configuration of the FDS that includes two recirculation pumps, but did not consider purging control.

In this paper, a fuel delivery including hybrid recirculation loops (ejector and blower) was designed as shown in Fig. 1. At a relatively low current demand, a low-pressure regulator is employed to independently supply the hydrogen and keep the inlet gas pressure nearly constant, while a blower is used to re-circulate hydrogen exhausted from the stack. At a relatively high current demand, a flow control valve is activated to supply additional hydrogen flow, and an ejector with a blower re-circulates the exiting hydrogen. The purge valve was opened and closed periodically to remove the excess liquid water and impurities in fuel cells.

In the following sections, all components in the FDS were modeled considering static or dynamic behavior, and then connected to the model of fuel cell stack. In fact, the three objectives defined for controls of the FDS are not significantly affected by the cathode side of stack. Therefore, only half a cell on the anode side was considered in the following study.

The integrated model is then used to develop a state feedback controller (SFB) with an observer, which was compared with other two classic controls such as the proportional and integral (PI) and static feed-forward (SFF) controller to analyze its tracking performance and disturbance rejection.

2. Modeling of the fuel delivery system

The FDS consists of three manifolds, ejector, supply, and return manifolds, an ejector, a blower, a pressure regulator, a flow control valve, and a purge valve as shown in Fig. 1. Several assumptions were made for development of models for the components:

(1) the outlet pressure of high-pressure regulator is stable;
(2) there is no pressure drop along the pipe connections;
(3) spatial variations are neglected in manifolds;
(4) no contaminant gases are in the hydrogen supplied by the tank;
(5) no gas crosses the membrane and no gas leaks in the fuel cell;
(6) the ideal gas law applies to all control volumes;
(7) all manifolds work in isothermal conditions;
(8) liquid water is not re-circulated by the blower or ejector; and
(9) gaseous and liquid water are in equilibrium state in all control volumes.

A block diagram for the integrated FDS is shown in Fig. 2, where the models for manifolds, blower and fuel cell stack consider dynamics, and others are static ones. The state variables in the dynamic models are written according to the block names.

2.1. Manifolds

As shown in Fig. 1, the ejector manifold is the part that connects the flow control valve and primary inlet of the ejector. The pressure dynamic of hydrogen in the ejector manifold is

$$\frac{dp_{em}}{dt} = \frac{R_{H_2} T_{em}}{V_{em}} (W_{fcv} - W_{ej,p}) \quad (1)$$

where p_{em} is the hydrogen pressure in ejector manifold, W_{fcv} is the mass flow rate of flow control valve and $W_{ej,p}$ is the mass flow rate of ejector primary inlet.

The water generated in cathode catalysts can be diffused across the membrane electrolyte assembly (MEA) to the gas flow channels

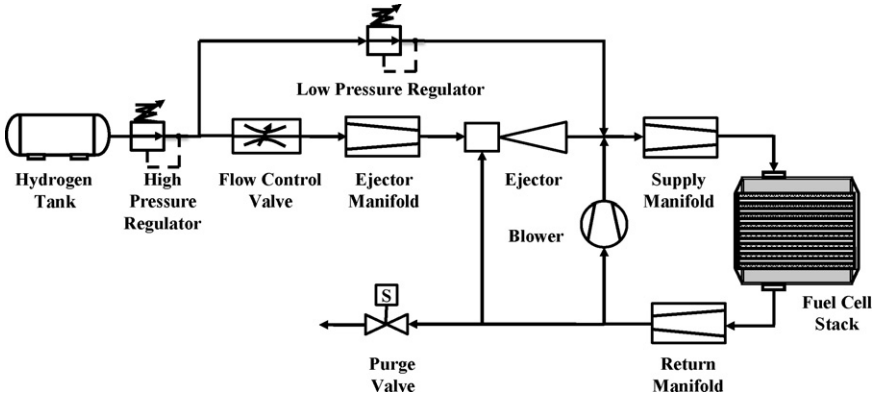

Fig. 1. Schematic diagram of fuel delivery and recirculation system.

of anode side, and then entrained by the gas flow in the channels, and transported to the return and supply manifolds. Thus, the hydrogen pressure and water activity dynamic equations are used to describe the mass balance in the manifolds [4]:

$$\frac{dp_{H_2,sm}}{dt} = \frac{R_{H_2}T_{sm}}{V_{sm}}(W_{H_2,lpr} + W_{H_2,ej,out} + W_{H_2,bl} - W_{H_2,sm,out}) \quad (2)$$

$$\frac{da_{w,sm}}{dt} = \frac{R_{H_2O}T_{sm}}{p_{sat}(T_{sm})V_{sm}}(W_{v,ej,out} + W_{v,bl} - W_{w,sm,out}) \quad (3)$$

where $p_{H_2,sm}$ is the hydrogen partial pressure in supply manifold; $W_{H_2,lpr}$, $W_{H_2,ej,out}$, and $W_{H_2,bl}$ are the mass flow rates of the low-pressure regulator, ejector outlet and blower.

The water activity a_w describes the total amount of water in gas and liquid phases in a control volume [4], and p_{sat} is the saturation pressure, which is a function of temperature of the control volume. $W_{v,ej,out}$ and $W_{v,bl}$ are the vapor mass flow rate of the ejector outlet and blower, and $W_{w,sm,out}$ is the total water mass flow rate (vapor and liquid water) at the outlet of the supplied manifold.

Likewise, dynamic equations that consider the two-phase water balance for the return manifold was derived:

$$\frac{dp_{H_2,rm}}{dt} = \frac{R_{H_2}T_{rm}}{V_{rm}}(W_{H_2,rm,in} - W_{H_2,ej,s} - W_{H_2,bl} - W_{H_2,purge}) \quad (4)$$

$$\frac{da_{w,rm}}{dt} = \frac{R_{H_2O}T_{rm}}{p_{sat}(T_{rm})V_{rm}}(W_{w,rm,in} - W_{v,ej,s} - W_{v,bl} - W_{w,purge}) \quad (5)$$

The water inflow rate of the return manifold, $W_{w,rm,in}$, and the water flow rate of purge valve, $W_{w,purge}$, are the total mass flow rates of vapor and liquid water.

The gas constant and specific heat capacity of the gas in the supply and return manifold are obtained by averaging the values of species (hydrogen and water vapor) based on the mass fraction. Then, the density and specific heat ratio of the mixed gas are obtained according to their definitions.

2.2. Ejector

Recent research [4–7] proposed ejectors as the anodic hydrogen recirculation pumps because of their simple structure, no moving

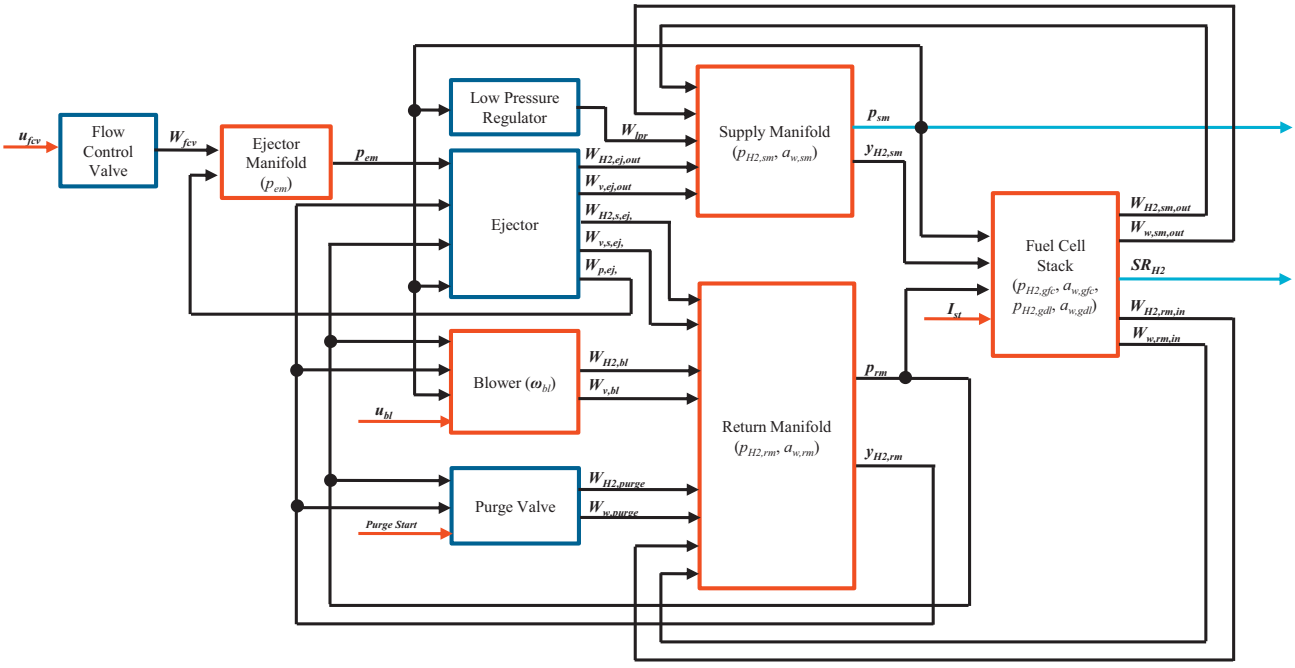

Fig. 2. Block diagram of integrated model of the FDS.

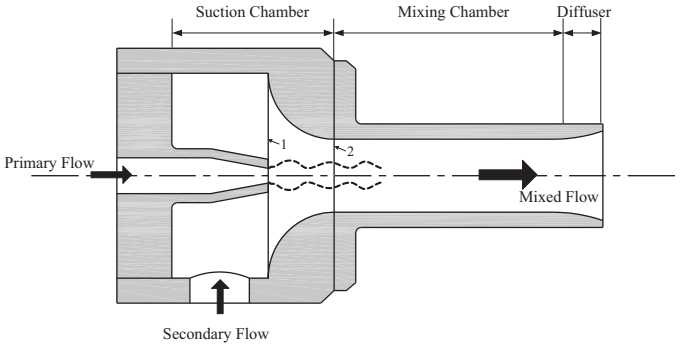

Fig. 3. Basic structure of an ejector.

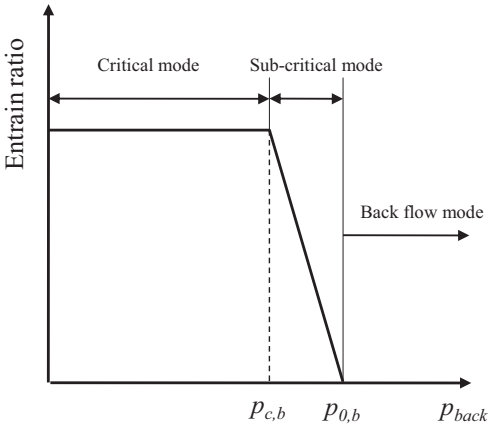

Fig. 4. Working mode of ejector.

parts, and no power consumption. The ejector allows the high pressure hydrogen to entrain the low pressure exhausting gas into the supply line.

The basic structure of an ejector is shown in Fig. 3. In critical mode, the high-pressure pure hydrogen of the primary flow is chocked at the throat of the primary inlet. The low-pressure hydrogen at the secondary inlet is entrained by high-speed primary flow. The mass flow rate at the primary inlet throat is described using the convergent nozzle equation [7]:

$$W_{ej,p} = \begin{cases} p_{em}A_{t,ej}\sqrt{\dfrac{\eta_{ej,p}\gamma_{H_2}}{R_{H_2}T_{em}}}\left(\dfrac{2}{\gamma_{H_2}+1}\right)^{(\gamma_{H_2}+1)/(2(\gamma_{H_2}-1))} & \text{if } \dfrac{p_{rm}}{p_{em}} \le \left(\dfrac{2}{\gamma_{H_2}+1}\right)^{1/(\gamma_{H_2}-1)} \\ p_{em}A_{t,ej}\sqrt{\dfrac{\eta_{ej,p}\gamma_{H_2}}{R_{H_2}T_{em}}}\left(\dfrac{p_{rm}}{p_{em}}\right)^{1/\gamma_{H_2}}\left\{\dfrac{2}{\gamma_{H_2}-1}\left[1-\left(\dfrac{p_{rm}}{p_{em}}\right)^{(\gamma_{H_2}-1)/\gamma_{H_2}}\right]\right\}^{1/2} & \text{if } \dfrac{p_{rm}}{p_{em}} > \left(\dfrac{2}{\gamma_{H_2}+1}\right)^{1/(\gamma_{H_2}-1)} \end{cases} \quad (6)$$

where $A_{t,ej}$ is the throat area, and $\eta_{ej,p}$ is the isentropic coefficient of primary flow. When the pressure ratio is less than a critical value (critical pressure ratio), the primary flow is choked, and the Mach number at the nozzle throat (section 1 in Fig. 3) is 1.

The primary flow and secondary flow mix at section 2 is shown in Fig. 3, where the static pressures of primary flow and secondary flow are identical. An exponential function along the direction of the radius is used to describe the velocity distribution at section 2. The mass flow rate of secondary flow in critical mode is [7]:

$$W_{c,s,ej} = \frac{2\pi\bar{\rho}_s U_{p,2}(R_2 - R_{p,2})(R_2 + R_{p,2} + n_v R_{p,2})}{(n_v+1)(n_v+2)} \quad (7)$$

where R_2 and $R_{p,2}$ are the radius of section 2 and primary flow at section 2, n_v is the exponent of the velocity function, and $\bar{\rho}_s$ is the average density of the secondary flow. The n_v is expressed as a function of pressures at the ejector inlet and geometric size of the ejector.

The above model assumes that the ejector is in critical mode, which implies that the entrain ratio (the mass flow rate ratio of secondary flow to primary flow) does not change with the backpressure as shown in Fig. 4. When the backpressure is higher than the critical pressure $p_{c,b}$, the ejector will work in a subcritical mode, and the entrain ratio will drop rapidly. If the backpressure is larger than the critical value $p_{0,b}$, the ejector will work in back flow mode.

The back flow mode of the ejector should be avoided in real applications. However, the ejector in the FDS may work in a subcritical mode. The critical backpressure, $p_{c,b}$, can be derived from the conservation equations of mixing and expansion processes in mixing and diffuser chambers, respectively [7]. When the backpressure becomes $p_{0,b}$ as shown in Fig. 4, the mass flow rate of the secondary flow becomes zero. The $p_{0,b}$, also can be calculated by using the conservation equations similar as the process of the calculation of $p_{c,b}$. Hence, the real mass flow rate of the secondary flow depending on the working modes or back pressure is derived from the linear interpolation as:

$$W_{s,ej} = \begin{cases} 0 & p_{sm} \ge p_{0,b} \\ W_{c,s,ej}\dfrac{p_{0,b}-p_{sm}}{p_{0,b}-p_{c,b}} & p_{c,b} < p_{sm} < p_{0,b} \\ W_{c,s,ej} & p_{sm} \le p_{c,b} \end{cases} \quad (8)$$

where p_{sm} is the supply manifold pressure that is considered as the backpressure of ejector. Then, the hydrogen and water vapor flow rates at the outlet of the ejector are:

$$W_{H_2,ej,out} = W_{ej,p} + W_{ej,s}y_{H_2,rm} \quad (9)$$

$$W_{v,ej,out} = W_{ej,s}(1 - y_{H_2,rm}) \quad (10)$$

2.3. Blower

The model of blower consists of two parts that describes a static characteristic of the blower and a dynamic behavior of electric motor. The static behavior of the blower is described by the dimensionless head parameter and scaled flow rate proposed by the Jensen & Kristensen method [8,9].

The dimensionless head parameter, Ψ_{bl}, is a function of the pressures and temperatures of blower inlet and outlet, and blower speed. The scaled flow rate, Φ_{bl}, is a function of blower mass flow rate. The relations of Ψ_{bl}, Φ_{bl} and blower efficiency η_{bl} proposed by Jensen & Kristensen method [9] are as follows:

$$\Phi_{bl} = \frac{a_1\Psi_{bl} + a_2}{\Psi_{bl} - a_3}, \quad \text{where } a_i = a_{i1} + a_{i2}M_{bl}, \quad i = 1, 2, 3 \quad (11)$$

$$\eta_{bl} = b_1\Phi_{bl}^2 + b_2\Phi_{bl} + b_3, \quad \text{where } b_i = \frac{b_{i1} + b_{i2}M_{bl}}{b_{i3} - M_{bl}}, \quad i = 1, 2, 3 \quad (12)$$

where a and b are the coefficients, and M_{bl} is the inlet Mach number defined by the blade tip velocity [9]. The parameters in Eqs. (11) and (12) are shown in Table 1.

Hence, the mass flow rate and blower efficiency are calculated by the pressures and temperatures of blower inlet and outlet, and

Table 1
Blower map function parameters.

a	Value	b	Value
a_{11}	-1.598×10^{-3}	b_{11}	−7923.8
a_{12}	2.663×10^{-2}	b_{12}	1.502×10^{4}
a_{21}	-3.062×10^{-2}	b_{13}	0.2144
a_{22}	−0.1740	b_{21}	24.91
a_{31}	14.55	b_{22}	−821.5
a_{32}	−15.73	b_{23}	-4.093×10^{-2}
		b_{31}	-4.929×10^{-2}
		b_{32}	0.8529
		b_{33}	1.715×10^{-2}

blower angular velocity that is the state variable of the dynamic blower model as:

$$\frac{d\omega_{bl}}{dt} = \frac{1}{J_{bl}}(\tau_{bm} - \tau_{bl}) \tag{13}$$

$$\tau_{bl} = \frac{c_{p,rm}T_{rm}}{\omega_{bl}\eta_{bl}}\left(\left(\frac{p_{sm}}{p_{rm}}\right)^{(\gamma_{g,rm}-1)/\gamma_{g,rm}} - 1\right) W_{bl}, \tau_{bm}$$
$$= \eta_{bm}\frac{k_t}{R_{bm}}(u_{bl} - k_v\omega_{bl}) \tag{14}$$

where J_{bl} is the rotational inertia of the rotator, η_{bm}, k_t, k_v and R_{bm} are motor parameters, and u_{bl} is the control voltage of the blower motor. The species (hydrogen and water vapor) flow rates of the blower can be calculated by the total and the species mass fraction in the return manifold.

2.4. Pressure regulator

As shown in Fig. 1, the low-pressure regulator is employed to stabilize the pressure of its outlet for a specific range of flow rates. The scaled mass flow rate, Φ_{lpr}, and the dimensionless pressure drop, Ψ_{lpr}, are introduced in the low-pressure regulator static model [4] as:

$$\Phi_{lpr} = \frac{W_{lpr}}{W_{lpr,max}} \quad \text{and} \quad \Psi_{lpr} = \frac{p_{lpr,set} - p_{lpr,out}}{p_{ref}} \tag{15}$$

where W_{lpr} is the mass flow rate of the low pressure regulator, $W_{lpr,max}$ is the maximum mass flow rate, $p_{lpr,set}$ is the setting pressure of the regulator, $p_{lpr,out}$ is the outlet pressure, and p_{ref} is the reference pressure (101,325 Pa). The scaled mass flow rate is assumed to be a polynomial function of a dimensionless pressure drop as:

$$\Phi_{lpr} = \min(1, -116.1\Psi^3 + 29.77\Psi^2 + 3.30\Psi + 0.077) \tag{16}$$

2.5. Flow control valve

The response of the flow control valve is fast enough, so that the relationship between the control signal and the flow rate is assumed to be linear:

$$W_{fcv} = u_{fcv}W_{fcv,max} \tag{17}$$

where u_{fcv} is the control input signal of the valve that varies from 0 to 1, and $W_{fcv,max}$ is the maximum mass flow rate.

2.6. Purge valve

The liquid water that accumulates in the return manifold is removed periodically by the purge valve as shown in Fig. 1. The flow rate through the nozzle of the purge valve is governed by the nozzle equation as Eq. (6), where the outlet pressure of the nozzle is the same as that of atmosphere. The species flow rates of hydrogen and vapor are:

$$W_{H_2,purge} = W_{purge}y_{H_2,rm} \tag{18}$$

$$W_{v,purge} = W_{purge}(1 - y_{H_2,rm}) \tag{19}$$

When the water activity in the return manifold is greater than one, liquid water will flow through the purge valve from the return manifold. The liquid water and the total water mass flow rate are obtained by:

$$W_{l,purge} = (a_{w,rm} - 1)W_{v,purge} \tag{20}$$

$$W_{w,purge} = W_{v,purge} + W_{l,purge} \tag{21}$$

3. Modeling of half a cell on anodic side

Performance of a cell is mainly determined by the reactions taking place in cathode side because of the lower reaction rate in the cathode than that in the anode. The role of the FDS is mainly to supply the sufficient hydrogen to stack, whereby the inlet fuel pressure is controlled at a given reference and liquid water present in channels is regularly removed. As the FDS mainly interacts with the anode side of the fuel cell, only behaviors of half a cell are considered in this study, which represents hydrogen consumptions, pressure and water flows.

A schematic diagram for mass transport of hydrogen and water in the half a cell is depicted in Fig. 5. The hydrogen supplied to the gas flow channels (GFC) diffuses through the gas diffusion layer (GDL) and reaches the catalyst layer (CL). Water is transported across the membrane between the anode and cathode, the amount of which is balanced by electro-osmotic force and back diffusion. The water vapor transported may be condensed in the channels or porous gas diffusion layer and then becomes a two-phase (water vapor and liquid water) flow that affects transport of reactant gas.

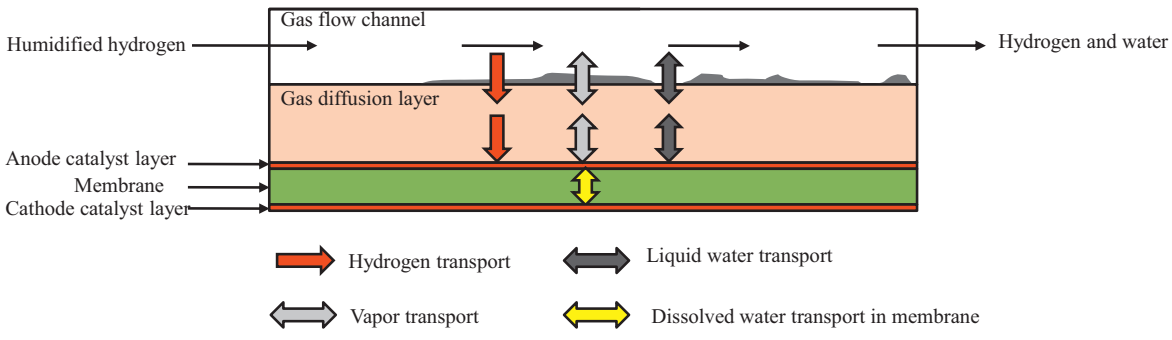

Fig. 5. Schematic diagram for mass transport in half a cell of anodic side.

3.1. Gas flow channels

The GFC in the fuel cell stack are regarded as one control volume without consideration of the spatial differences. The dynamics of hydrogen partial pressure and water activity in the GFC of single cell are described by:

$$\frac{dp_{H_2,gfc}}{dt} = \frac{R_{H_2}T_{st}}{V_{gfc}}(W_{H_2,gfc,in} - j_{H_2,gfc,gdl}A_{act} - W_{H_2,gfc,out}) \quad (22)$$

$$\frac{da_{w,gfc}}{dt} = \frac{R_{H_2O}T_{st}}{p_{sat}(T_{st})V_{gfc}}(W_{w,gfc,in} + j_{w,gfc,gdl}A_{act} - W_{w,gfc,out}) \quad (23)$$

where $p_{H_2,gfc}$ and $a_{w,gfc}$ are the hydrogen partial pressure and water activity in the GFC, T_{st} is the stack temperature, and V_{gfc} is the total volume of the anode GFC in the single cell.

The inlet mass flow rates of hydrogen and water vapor are calculated by the pressure difference between the supply manifold and GFCs as:

$$W_{H_2,gfc,in} = k_{gfc,in}A_{gfc,in}\rho_{H_2,sm}(p_{sm} - p_{gfc}) \quad (24)$$

$$W_{v,gfc,in} = k_{gfc,in}A_{gfc,in}\rho_{v,sm}(p_{sm} - p_{gfc}) \quad (25)$$

where $k_{gfc,in}$ is the flow coefficient at the inlet of the GFC, $A_{gfc,in}$ is the inlet area of the GFC of a single cell, and the total pressure in the GFC, p_{gfc} is calculated by the hydrogen partial pressure and water activity.

In realty, the pressure drop along the GFC depends on geometrical dimensions and operating conditions that include the cross-section shape of the channels, contact angles and surface roughness on the channel walls, the channel patterns such as serpentine, inter-digitized or straight, gas properties, amount of liquid water and flow patterns.

In current model, the $p_{sm} - p_{rm}$ is considered as the total pressure drop along the GFC. The total pressure drop is divided into two parts, inlet pressure drop $p_{sm} - p_{gfc}$ and outlet pressure drop $p_{gfc} - p_{rm}$. The relationship between the pressure drop and flow rate is further simplified using a constant inlet flow coefficient $k_{gfc,in}$ (Eq. (25)). This flow coefficient is determined by the channel conditions such as cross section, channel wall condition and patterns. Effects of liquid water effect are neglected in the inlet flow coefficient because little water is expected to be present in the inlet part of the GFC. At the outlet, a similar outlet flow coefficient is applied, but effects of liquid water are considered using the relationship given between flow rate and pressure drop described in the following sections.

If no purging takes place, no liquid water flows to the stack from the supply manifold. Otherwise, the liquid water entering the GFCs of a single cell is

$$W_{l,gfc,in} = (a_{w,sm} - 1)W_{v,gfc,in} \quad (26)$$

If the water activity in the supply manifold is less than 1, no liquid water exists in the manifold and the $W_{l,gfc,in}$ is 0. Then, the total water mass flow rate entering a single cell $W_{w,gfc,in}$ in Eq. (23) is equal to the sum of $W_{v,gfc,in}$ and $W_{l,gfc,in}$.

The total inlet flow rates of multiple cells of a stack are equal to the total mass flow rate leaving the supply manifold:

$$W_{H_2,sm,out} = N_{cell}W_{H_2,gfc,in}, \qquad W_{w,sm,out} = N_{cell}W_{w,gfc,in} \quad (27)$$

Similarly, the mass flow rates of gas species at the outlet of GFCs is

$$W_{H_2,gfc,out} = k_{gfc,out}A_{gfc,out}\rho_{H_2,gfc}(p_{gfc} - p_{rm}) \quad (28)$$

$$W_{v,gfc,out} = k_{gfc,out}A_{gfc,out}\rho_{v,gfc}(p_{gfc} - p_{rm}) \quad (29)$$

where $k_{gfc,out}$ is the outlet flow coefficient that is not a constant. In the model, the amount of liquid water is considered as the dominant variable that affects the relationship of outlet pressure drop and flow rate. Increase of liquid water in the channels leads to an increase of the flow resistance and as a result the flow coefficient becomes smaller. The flow coefficient at the outlet of the GFC can be described as:

$$k_{gfc,out} = k_{gfc,in}(1 - s_{gfc})^{1.5} \quad (30)$$

where s_{gfc} is the liquid water saturation, which is defined as the liquid volume fraction in the control volume, and calculated by:

$$s = \frac{\rho_{sat}(a_w - 1)}{\rho_l - \rho_{sat}} \quad (31)$$

where ρ_{sat} is the density of saturated vapor calculated by the saturation pressure and temperature in the control volume.

The liquid water in the outlet of the fuel cell stack is entrained by the viscous force of the gas flow in the channels. The mass flow rate, $W_{l,gfc,out}$, is expressed as:

$$W_{l,gfc,out} = C_{tp,gfc}\rho_l A_{gfc,out}\left(\frac{s_{gfc}}{1 - s_{gfc}}\right)^2 \frac{\mu_{g,gfc}}{\mu_l}U_{g,gfc,out} \quad (32)$$

where $C_{tp,gfc}$ is the correction factor, $\mu_{g,gfc}$ and μ_l are the viscosity of gas in GFC and liquid water, and $U_{g,gfc,out}$ is the superficial velocity of gas at the outlet of the channel.

The viscosity of the mixed gas of hydrogen and vapor is obtained by the average value given by the semi-empirical formula proposed by Wilke [10], and the superficial gas velocity is given by:

$$U_{g,gfc,out} = k_{gfc,out}(p_{gfc} - p_{rm}) \quad (33)$$

Then, the water mass flow rate of a single cell at its outlet is the sum of the flow rates of water vapor and liquid water. Then, the total mass flow rates exhausted from all cells of the stack are:

$$W_{H_2,rm,in} = N_{cell}W_{H_2,gfc,out}, \qquad W_{w,rm,in} = N_{cell}W_{w,gfc,out} \quad (34)$$

Now, unknown variables in the dynamic equations, Eqs. (22) and (23), are the species fluxes between the GFC and gas diffusion layer that are derived in the following section.

3.2. Gas diffusion layers

For the model of GDL, the volume of pores in the GDL is considered as an isothermal control volume. Then, the dynamics for the GDL are described as follows:

$$\frac{dp_{H_2,gdl}}{dt} = \frac{R_{H_2}T_{st}}{(1 - s_{gdl})\varepsilon_{gdl}\delta_{gdl}}(j_{H_2,gfc,gdl} - j_{H_2,gdl,cl}) \quad (35)$$

$$\frac{da_{w,gdl}}{dt} = \frac{R_{H_2O}T_{st}}{p_{sat}(T_{st})\varepsilon_{gdl}\delta_{gdl}}(j_{v,gfc,gdl} + j_{l,gfc,gdl} - j_{v,gdl,cl} - j_{l,gdl,cl}) \quad (36)$$

where ε_{gdl} is the porosity of the GDL, δ_{gdl} is the thickness of the layer and j is the mass flux through the layer.

The hydrogen and water vapor fluxes from the GFC to the GDL are calculated using the Fick's law as:

$$j_{[\,],gfc,gdl} = h_{m,gfc,gdl}(C_{[\,],gfc} - C_{[\,],gdl}) \quad (37)$$

where $C_{[\,],gfc}$ and $C_{[\,],gdl}$ refer to the concentrations of gas species in the GFC and GDL and are obtained by the hydrogen partial pressure and water activity. The mass transfer coefficient between GFC and GDL is given by:

$$h_{m,gfc,gdl} = \frac{h_{m,gfc}h_{m,gdl}}{h_{m,gfc} + h_{m,gdl}} \quad (38)$$

where the mass transfer coefficients in GFC and GDL are:

$$h_{m,gfc} = \frac{A_{gfc,gdl}(1 - r_{A,cover})}{A_{act}} \frac{Sh_{gfc} D_{H_2-H_2O,gfc}}{d_{h,gfc}},$$

$$h_{m,gdl} = \frac{2D_{H_2-H_2O,gdl}}{\delta_{gdl}} \tag{39}$$

where the $A_{gfc,gdl}$ is the area of gas contact interface between GFC and GDL for single cell, A_{act} is the active area of the fuel cell, Sh_{gfc} is the Sherwood number of the channels, $d_{h,gfc}$ is the channel hydraulic diameter, and $r_{A,cover}$ is the liquid water cover ratio on the gas contact interface between GFC and GDL, that is defined and calculated as:

$$r_{A,cover} = \frac{A_{liquid,gfc,gdl}}{A_{gfc,gdl}} = \min[1, K_{cover}(1 - s_{gfc})] \tag{40}$$

where $A_{liquid,gfc,gdl}$ is the liquid water cover area on the interface between the GFC and GDL. The binary diffusion coefficient $D_{H_2-H_2O}$ in Eq. (39) is [11]:

$$D_{H_2-H_2O} = \begin{cases} K_{H_2-H_2O}\left(\dfrac{T^{1.5}}{p}\right) & \text{for GFC} \\ K_{H_2-H_2O}\varepsilon^{1.5}(1-s)^{2.5}\left(\dfrac{T^{1.5}}{p}\right) & \text{for GDL and CL} \end{cases} \tag{41}$$

where $K_{H_2-H_2O}$ is a constant, ε is the porosity of layers, s is the liquid saturation, T is the temperature (K) and p is the pressure (Pa).

Since the CL is much thinner than that of the GDL, the characteristic diffusion time in the CL given by δ^2/D is also much shorter than that in the CLs. Thus, the CL is considered as the boundary for both the GDL and membrane. According to the mass conservation principle, the hydrogen flux from the GDL to the CL is equal to that consumed in the CL as:

$$j_{H_2,gdl,cl} = \frac{M_{H_2O}}{2F} I_{den} \tag{42}$$

where $I_{den} = I_{st}/(N_{cell}A_{act})$ is the area current density of the fuel cell stack.

The vapor transfer from the GDL to the CL is given by:

$$j_{v,gdl,cl} = h_{m,gdl,cl}(C_{v,gdl} - C_{v,cl}) \tag{43}$$

where C_v is the vapor concentration obtained from the water activity.

Liquid water transport at the interface between the GDL and GFC is driven by the capillary pressure in pores. The liquid water flux is determined by the difference between the critical pressure in the GFC and the capillary pressure in GDL:

$$j_{l,gfc,gdl} = h_{l,cap,gdl}(p_{c,crit} - p_{c,gdl}) \tag{44}$$

where $h_{l,cap,gdl}$ is the liquid water transfer coefficient in GDL, and $p_{c,gdl}$ is the capillary pressure in the GDL written as:

$$h_{l,cap,gdl} = -\frac{2\rho_l K_{gdl} K_{r,gdl}}{\delta_{gdl}\mu_l} \tag{45}$$

$$p_c = \sigma_w \cos\theta_c \sqrt{\frac{\varepsilon}{K}}(1.417S - 2.12S^2 + 1.263S^3) \tag{46}$$

where K is the permeability, K_r is the relative permeability, σ_w is water surface tension, θ_c is contact angle, and S is the reduced liquid saturation. The K_r and S can be written as:

$$K_r = (s - s_{im})^3, \qquad S = \frac{s - s_{im}}{1 - s_{im}} \tag{47}$$

where s_{im} is the immobile liquid saturation.

Likewise, the mass flux of liquid from the GDL to the CL is determined by the capillary pressure difference between these two layers, given by:

$$j_{l,gdl,cl} = h_{l,cap,cl}(p_{c,gdl} - p_{c,cl}) \tag{48}$$

where $p_{c,cl}$ is the capillary pressure in the CL, and $h_{l,cap,cl}$ is the liquid water transfer coefficient at the boundary of GDL near the CL, where it is assumed that the capillary pressure is continuous as:

$$p_{c,gdl,cl} = p_{c,cl} \tag{49}$$

where $p_{c,gdl,cl}$ is the capillary pressure of GDL at the boundary near the CL. Now, if the capillary pressure $p_{c,cl}$ is known, the reduced liquid saturation of GDL near the CL, $S_{gdl,cl}$ is calculated from $p_{c,gdl,cl}$ by using the inverse function of Eq. (46), and as a result the liquid water transfer coefficient at the boundary of GDL near CL, $h_{l,cap,cl}$, is obtained using Eqs. (45) and (47).

Now, the mass flow rates of gas species and liquid water at both the boundaries of GDL in Eqs. (35) and (36) are calculated by using Eqs. (37), (42), (43), (44) and (48). The unknown variables in these equations are the water vapor concentration, $C_{v,cl}$, and capillary pressure, $p_{c,cl}$, in the CL that are a function of the water activity in the CL. The water activity in the CL can be calculated by the water balance in the GDL, CL and membrane described in following section.

3.3. Membrane

Because of the thin thickness of the CL, the boundary between the GDL and the membrane, the water flux across the CL is assumed to be continuous and described as follows:

$$j_{v,gdl,cl} + j_{l,gdl,cl} = \frac{\alpha_{drag} M_{H_2O}}{F} I_{den} + \frac{M_{H_2O}\rho_{pem} D_\lambda}{\delta_{pem} EW_{pem}}(\lambda_{an} - \lambda_{ca}) \tag{50}$$

Hence, the terms on the left are the total water mass flux from the GDL to the CL. The terms on the right are the total water flux from the CL to the membrane, where the first one represents the water flux driven by the electro-osmotic drag force, and the second one is that driven by the gradient of the water content in membrane. The electro-osmotic drag coefficient is [12]:

$$\alpha_{drag} = \begin{cases} \lambda_{an} & \lambda_{an} \le 1 \\ 1 & 1 < \lambda_{an} \le \lambda_v^{max} \\ 1.5\dfrac{\lambda_{an} - \lambda_v^{max}}{\lambda_l^{max} - \lambda_v^{max}} + 1 & \lambda_{an} > \lambda_v^{max} \end{cases} \tag{51}$$

where λ_{an} is the water content of the membrane near the anode CL, λ_v^{max} is the equilibrium maximum water content when the membrane contacts with saturated water vapor only ($a_{w,cl} = 1$), and λ_l^{max} is the maximum value of when the membrane contacts liquid water.

The equilibrium water content near the CL is expressed as a function of the water activity of the CL at different temperatures obtained from the experimental data [13,14] as:

$$\begin{aligned} \lambda_{[30\,^\circ C]} &= \begin{cases} 0.04 + 17.81a_w - 39.85a_w^2 + 36.0a_w^3 & a_w \le 1 \\ 14 + 8(a_w - 1) & 1 < a_w \le 3 \\ 22 & a_w > 1 \end{cases} \\ \lambda_{[80\,^\circ C]} &= \begin{cases} 0.3 + 10.8a_w - 16a_w^2 + 14.116a_w^3 & a_w \le 1 \\ 9.216 + 3.792(a_w - 1) & 1 < a_w \le 3 \\ 16.8 & a_w > 1 \end{cases} \end{aligned} \tag{52}$$

Thus, the water content for other values of temperature is obtained by interpolating the function values above at given specific water activity as [15]:

$$\lambda[a_w, T] = (\lambda_{[80\,^\circ C]}[a_w] - \lambda_{[30\,^\circ C]}[a_w])\frac{T - 303.15}{50} + \lambda_{[30\,^\circ C]}[a_w] \tag{53}$$

where T is the temperature (K) of the CL. The water content functions are shown in Fig. 6, where the curve of water content at 60 °C is obtained by an interpolation from the curves of water content at 30 °C and 80 °C.

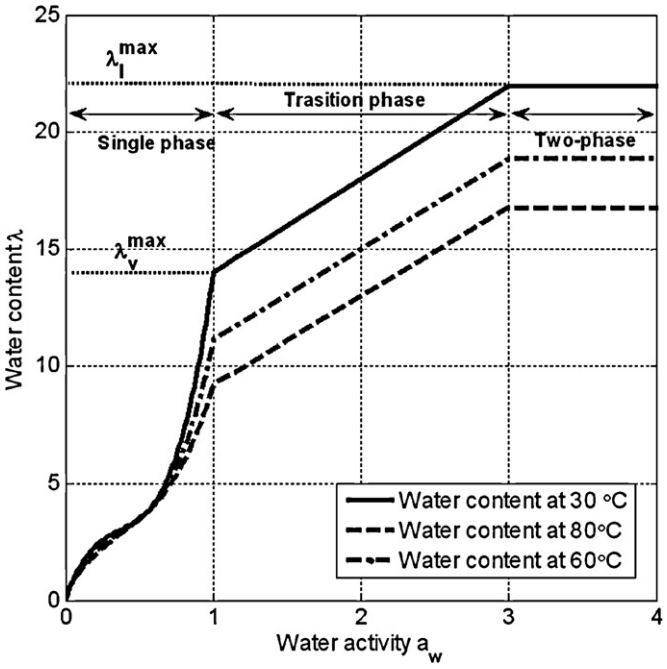

Fig. 6. Water content function for different temperatures.

From Eqs. (52) and (53), the water content curve is divided into three phases as shown in Fig. 6. The transition phase of the curve is used to remove the discontinuity of the water content curve at the saturation point ($a_w = 1$). The λ_v^{max} and λ_l^{max} are the water content values at the water activity $a_w = 1$ and $a_w \geq 3$, respectively.

In Eq. (50), the diffusion coefficient of dissolved water in membrane, D_λ can be described as a function of the water content of anode side as [16]:

$$D_\lambda = \begin{cases} 3.1 \times 10^{-7} \lambda_{an}(e^{0.28\lambda_{an}} - 1)e^{-2436/T_{st}} & \lambda_{an} \leq 3 \\ 4.17 \times 10^{-8} \lambda_{an}(161e^{-\lambda_{an}} + 1)e^{-2436/T_{st}} & \text{else} \end{cases} \quad (54)$$

In fact, water is mostly generated in the cathode CL. Thus, the water content of the membrane near the cathode CL λ_{ca} in Eq. (50) is assumed to be the liquid maximum value λ_l^{max} that is a function of stack temperature by Eq. (53) with $a_w = 3$. Hence, the right hand side of Eq. (50) is a function of water activity in the anode CL when the current density I_{den} and stack temperature T_{st} are known. Then, the water flux across the membrane and the water activity in the anode CL can be solved by substituting Eqs. (43) and (48) into left hand side of Eq. (50).

All components along with the fuel cell mode are shown in Fig. 7. The whole fuel cell system includes four state variables, and the input variables are the gas states in the supply manifold, return manifold and stack current.

4. Analysis of integrated system of FDS and stack

Design of controllers for the FDS is carried out for three operating modes, separately, dependent upon magnitude of currents requested; low, medium and high currents. The low, medium, and high currents refer to a current density range of 0–6000 A m^{-2}, 6000–8000 A m^{-2}, and above 8000 A m^{-2}, respectively.

In the low current mode, the flow control valve and ejector are closed, and the low-pressure regulator is used to control supply of the hydrogen while the blower works as a pump to re-circulate the exhausted hydrogen. For medium and high current mode, both flow control valve and ejector are used to supply and re-circulate more hydrogen.

Likewise, controls of anode gas pressure and flow rate are carried out differently. In the low current mode, a low pressure regulator is used to passively stabilize the pressure near its reference value while the blower is used to actively adjust the recirculation mass flow rate to control the total flow rate of hydrogen feeding to the fuel cell stack. In medium and high current modes, the flow control valve and blower are two actuators to control the pressure and hydrogen flow rates supplied to stack simultaneously. In all modes, the stack current and purging operations are considered as disturbances.

The integrated model along with two PI controllers for flow control valve and blower is used to find out values for steady states. Results of simulations show that the water activities in supply and return manifolds cannot reach steady states because of the continuous phase change between liquid water and water vapor in the manifolds. Thus, it is assumed that the manifolds are fully saturated to get other steady state values. On the other hand, the supply manifold pressure, p_{sm} (bar) for medium and high current mode is assumed to be a function of current density as:

$$p_{sm} = 1.49 + 2 \times 10^{-6}(I_{den} - 6000) \quad (55)$$

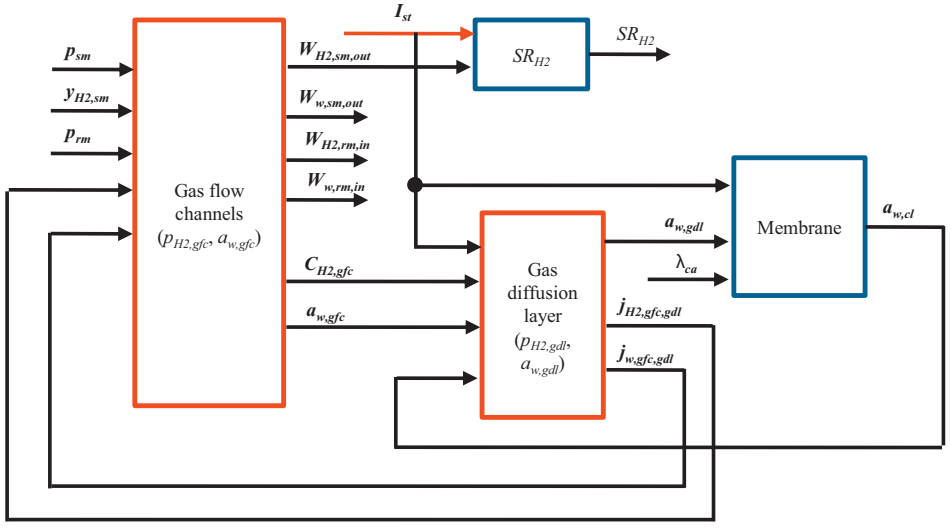

Fig. 7. Block diagram of integrated model of fuel cell stack.

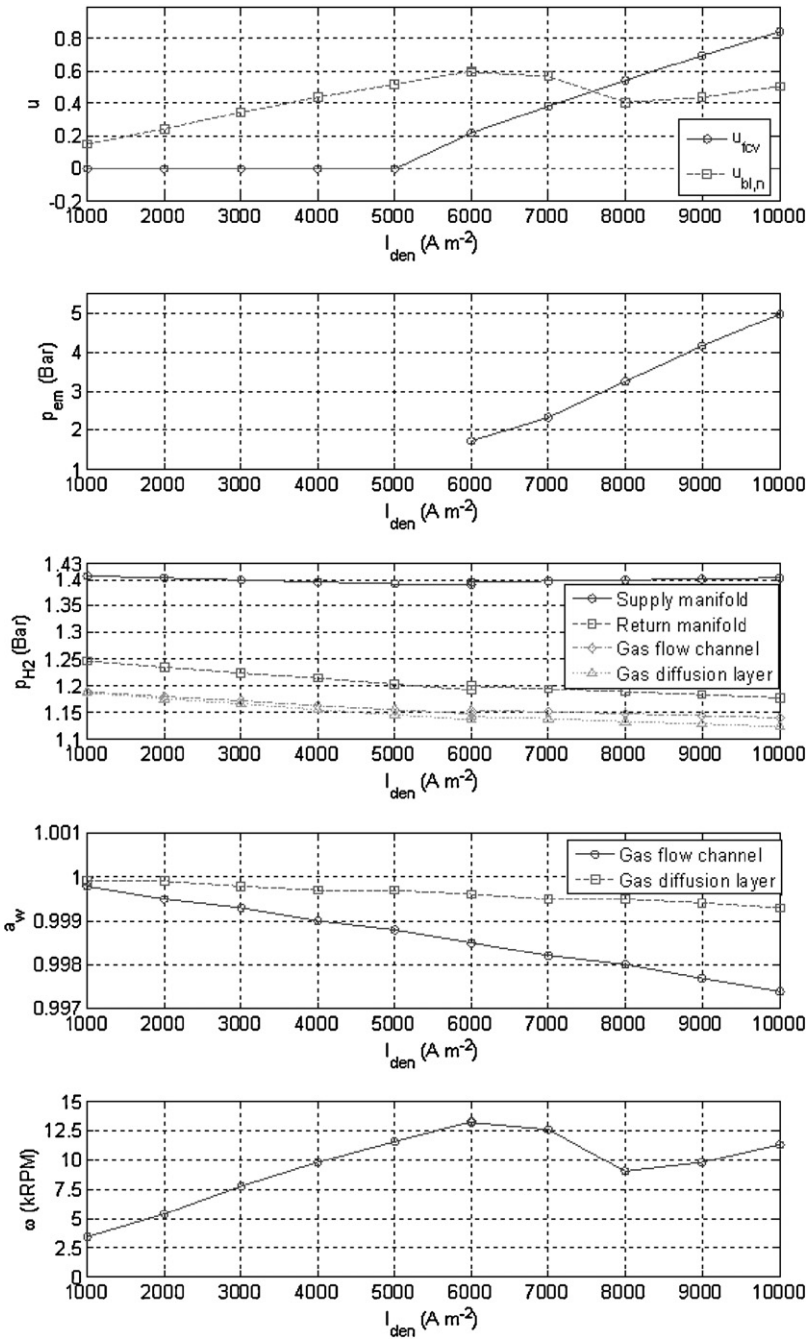

Fig. 8. Control inputs and state variables at steady state at different current densities.

The stoichiometric ratio of hydrogen (SR_{H_2}) instead of the flow rate, of the supplied hydrogen, is defined as the ratio of hydrogen flow rate entering the stack to that consumed by reactions. In this paper, the reference for SR_{H_2} is set as a constant 1.5 for all three modes.

Ten operating points including the steady state variables and control signals are obtained for different current densities (from 1000 to 10,000 A m^{-2} by step of 1000 A m^{-2}) as shown in Fig. 8 with the parameters in Table 2. The range of control signal for the blower, u_{bl}, is from 0 to 350 V, which is normalized from 0 to 1.

In Fig. 8, the control voltage and the angular velocity of the blower increase when current density is in low current mode, but decrease in the medium current mode and then increase in high current mode. When the recirculation takes place in the ejector in medium and high current mode, the power of the blower dissipated gets decreased because of the recirculation. Based on steady state analysis, a static feed-forward (SFF) control was proposed, where the control signals are directly derived from the current density [4].

5. Design of state feed-back control with an observer

When the load for the stack is in a low current mode, the supply line of the flow control valve and ejector recirculation is closed, so the FDS is operated with one supply line and one recirculation loop. This operation can be regarded as a single input and single output (SISO) control system. The SR_{H_2} can be simply controlled using a PI controller with gains ($K_{P,SR} = 3$, $K_{I,SR} = 6$).

Table 2
Model parameters.

Symbol	Value	Symbol	Value
$W_{fcv,max}$	2.4×10^{-3} kg s^{-1}	T_{st}	353 K
V_{em}	2.5×10^{-3} m^3	δ_{gdl}	250 μm
T_{em}	293 K	ε_{gdl}	0.6
$A_{t,ej}$	8.04×10^{-6} m^2	$\theta_{c,gdl}$	110°
$A_{m,ej}$	4.07×10^{-5} m^2	K_{gdl}	1.76×10^{-11} m^2
η_p	0.64	ρ_{pem}	2×10^3 kg m^{-3}
η_s	0.9	δ_{pem}	60 μm
η_{exp}	0.60	EW_{pem}	1.1 kg mol^{-1}
η_{mix}	0.90	$p_{c,crit}$	800 Pa
$p_{set,lpr}$	1.5×10^5 Pa	J_{bl}	2.6×10^{-3} kg m^2
$W_{lpr,max}$	1.75×10^{-3} kg s^{-1}	k_t	0.15 N m A^{-1}
V_{sm}	4×10^{-3} m^3	k_v	0.15 V rad^{-1} s
T_{sm}	318 K	R_{bm}	0.82 ohm
V_{rm}	4×10^{-3} m^3	η_{bm}	0.9
T_{rm}	338 K	D_{bl}	0.15 m
N_{cell}	381	ρ_l	986 kg m^{-3}
A_{act}	576 cm^2	σ_w	6.25×10^{-2} N m^{-1}
$A_{gfc,in}$	8 mm^2	K_{D_0,H_2-H_2O}	1.7232×10^{-3}
$A_{gfc,gdl}$	288 cm^2	$C_{tp,gfc}$	0.5
s_{im}	0.01	K_{cover}	1.5
Sh_{gfc}	2.78	$A_{t,purge}$	5×10^{-6} m^2
$k_{gfc,in}$	0.002 m s^{-1} Pa^{-1}	η_{purge}	0.81
V_{gfc}	2.8×10^{-5} m^3		

When the load for the stack is in the medium and high current mode, controls of the FDS is not as simple as that in the low current mode because of involvement of the ejector and blower along with two phase phenomena. Thus, the complete FDS with the stack is described in the form of state equations as:

$$\begin{cases} \dot{x} = f(x, u, w) \\ y = g(x, u, w) \\ z = h(x, u, w) \end{cases} \tag{56}$$

where x is the vector of state variables, u is the vector of control inputs, w is the vector of disturbance inputs, y is the vector of measurable outputs and z is the vector of control objectives.

$$\begin{cases} x = (p_{em}, p_{H_2,sm}, a_{w,sm}, p_{H_2,rm}, a_{w,rm}, \omega_{bl}, p_{H_2,gfc}, a_{w,gfc}, p_{H_2,gdl}, a_{w,gdl})^T \\ z = (p_{sm}, SR_{H_2}) \\ u = (u_{fcv}, u_{bl}) \\ w = I_{st} \end{cases} \tag{57}$$

The hydrogen pressure in supply manifold is considered as another control variable that should follow the pressure at cathode side. Simulation results using the PI controller show that the water activities in supply and return manifolds do not converge and increase slowly with time, while the water activities in the GFC and the GDL remains almost 1, which is unobservable. Thus, the dynamics of water activities cannot be considered in designing of controllers and are assumed to be constant 1. Likewise, the hydrogen pressure in the GDL is also unobservable. Thus, the state vector is simplified as follows:

$$x = (p_{em}, p_{H_2,sm}, p_{H_2,gfc}, p_{H_2,rm}, \omega_{bl})^T \tag{58}$$

where the pressures are in the units of bar, and the angular velocity of blower ω_{bl} is in units of kRPM.

The measurable output vector y in Eq. (56) for the controller design in medium and high modes is as:

$$y = (p_{em}, p_{sm}, p_{rm}, \omega_{bl}, Q_{sm,out})^T \tag{59}$$

where the pressures p_{em}, p_{sm} and p_{rm} are in the unit of bar, and $Q_{sm,out}$ is the flow rate at the outlet of the supply manifold in the units of SLPM, which is also the flow rate entering the stack $Q_{st,in}$.

The values of blower angular velocity and other states at steady state for different stack current densities are shown in Figs. 8 and 9. Other steady state values of the vector y are obtained by interpolating these curves.

In the vector z, the SR_{H_2} at the inlet of the fuel cell is not measurable directly and estimated by the $Q_{sm,out}$ as:

$$SR_{H_2} = \frac{Q_{sm,out}}{Q_{H_2,reacted}} \frac{p_{sm} - 1 \times 10^{-5} p_{sat}(T_{sm})}{p_{sm}}, \tag{60}$$

where p_{sm} (bar) is the total pressure in supply manifold, $Q_{H_2,reacted}$ (SLPM) is the rate of hydrogen consumption obtained from the $W_{H_2,reacted} = N_{cell} M_{H_2} I_{st}/(2F)$.

A block diagram for a state feed-back controller designed is depicted in Fig. 10, where the cathode pressure and SR_{H_2} are the

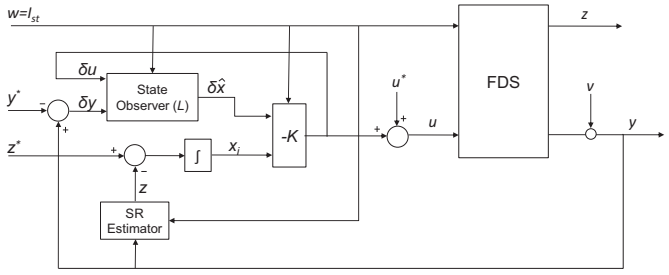

Fig. 10. Block diagram for state feedback control with integral and observer.

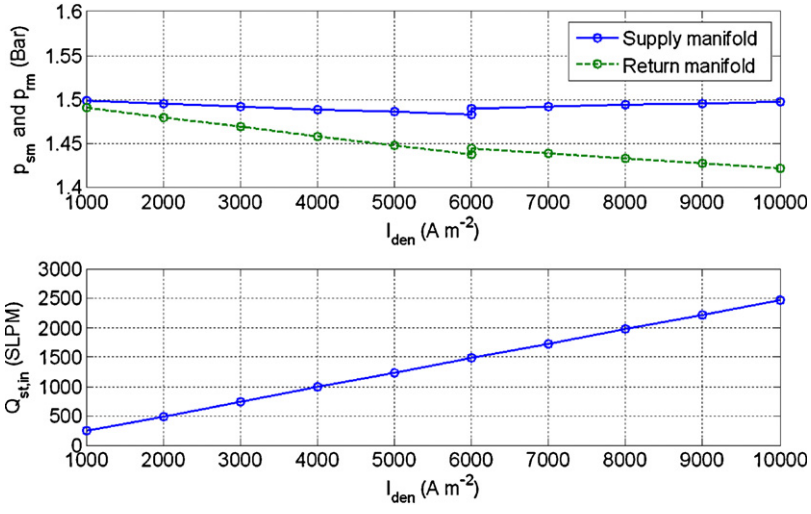

Fig. 9. Measurable outputs at steady state at different current density.

state variables to track. u^* and y^* are the steady state values that are calculated by the feed forward block, and z^* is the reference vector of the p_{sm} and SR_{H_2}. The SR estimator block outputs the p_{sm} directly measured by a sensor, and SR_{H_2} that is obtained by Eq. (60). A state observer is designed to estimate perturbations of the state variables of the system. The K and L are the controller gains and observer gains determined by using the Linear-Quadratic-Gaussian (LQG) method.

The state equation above for the FDS and stack is nonlinear and needs to be linearized for design of controllers and observers. Operating points for the systems are chosen at two currents, $I_{den} = 7000\ A\ m^{-2}$ and $I_{den} = 9000\ A\ m^{-2}$, that represent the medium and high current mode. Thus, two linear equations are obtained for each of the modes. At these operating points, the linearized system of FDS is written in the form of state equations as:

$$\begin{cases} \delta\dot{x} = A\delta x + B_u\delta u + B_w\delta w \\ \delta y = C\delta x + D_u\delta u + D_w\delta w \\ \delta z = G\delta x + H_u\delta u + H_w\delta w \end{cases} \quad (61)$$

where $\delta(\,) = (\,)_{op} - (\,)$ is a perturbation describing the difference between the state variables and their steady state values at the operating points, and the A, B_u, B_w, C, D_u, D_w, G, H_u and H_w are the system matrices. For the medium and high modes, the two linear dynamic models are obtained to calculate the controller and observer gains.

The SFB control is designed based on the Linear-Quadratic-Integral control as shown in Fig. 10:

$$u = -K[x; x_i] \quad (62)$$

where the x_i is the integrator output.

The controller gain K is optimized using the method of Linear Quadratic Regulator (LQR) that minimizes the cost function that is defined as:

$$J = \int_0^\infty (\delta z^T Q_z \delta z + x_i^T Q_i x_i + \delta u^T R \delta u)\,dt \quad (63)$$

where Q_z, Q_i and R are the weighting matrices for the control objectives, error integral and control inputs.

The same weighing matrices of the cost function are used for the controller design in the systems of medium and high current modes, which are given as:

$$\begin{cases} Q_z = \mathrm{diag}([1\times10^8, 1\times10^6]) \\ Q_i = \mathrm{diag}([1\times10^{10}, 1\times10^8]) \\ R = \mathrm{diag}([1\times10^2, 1\times10^4]) \end{cases} \quad (64)$$

where the matrices are all in diagonal form. The gains K are calculated using the MATLAB command, $K = \mathrm{lqi}(\mathrm{ss}(A, B_u, G, H_u), Q, R)$, where $Q = \mathrm{blkdiag}(C^T Q_z C, Q_i)$ is a 5-by-5 block diagonal matrix. The calculation results for the medium and high current mode are:

$$K_{mid} = \begin{bmatrix} 27.007 & 710.78 & -1587.7 & -328.47 & 1.9046 & -3177.8 & -948.16 \\ 0.41694 & 5.6295 & -47.315 & -13.965 & 0.093718 & 948.16 & -31.778 \end{bmatrix}$$
$$K_{high} = \begin{bmatrix} 7.0309 & 229.32 & -189.96 & 40.8 & 1.3737 & -9616 & -274.46 \\ 0.30072 & 15.957 & -86.847 & -16.357 & 0.4293 & 274.46 & -96.16 \end{bmatrix} \quad (65)$$

The linear observer shown in Fig. 10 estimates states perturbation $\delta\hat{x}$ using perturbations δu and $\delta y = y - y^*$ as input, which is described as follows:

$$\frac{d\delta\hat{x}}{dt} = A\delta\hat{x} + B_u + L(\delta y - C_u\delta\hat{x} - D_u u) \quad (66)$$

where A, B_u, C, and D_u are the linear system matrices in Eq. (61). To minimize effects of noises on the measuring outputs and states to be estimated, the Kalman filter is employed to obtain the observer gain matrix L. Covariance of process and measurement noises e for different currents is given as $Q_n = 10$ and $R_n = \mathrm{diag}([1\times10^{-4}, 1\times10^{-4}, 1\times10^{-4}, 1\times10^{-4}, 1])$. Then, the observer gains L (5-by-5 matrix) for both modes are calculated by the MATLAB command $[k_{est}, L, P] = \mathrm{kalman}(\mathrm{ss}(A, [B_u, B_w], C, [D_u, D_w]), Q_n, R_n)$.

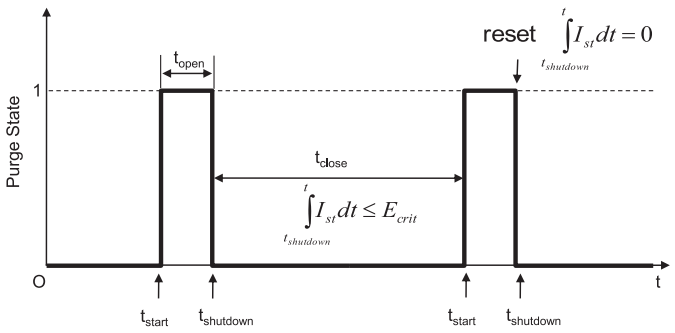

Fig. 11. State of purge valve.

Another disturbance that should be considered for design of the controllers is the purging operation. This operation is required to prevent accumulation of inert gases and remove impurities that decrease output voltage.

The purging is a dynamic process, which is determined by concentrations of impurities and liquid water volume in the system and controlled by two parameters, a purge on-time and purge off-time [17]. At a stable SR_{H_2}, concentration of the impurities and the liquid water volume is proportional to the amount of hydrogen consumed that is calculated by integrating the stack current. Thus, control strategy of the purging process of the FDS is dependent on integration of the stack current as:

$$\begin{cases} \text{Open the purge valve if } \int_{t_{shutdown}}^{t} I_{st}\,dt > E_{crit} \\ \text{Shutdown the purge valve after it opens for time length of } t_{open} \end{cases} \quad (67)$$

where E_{crit} is a constant that should be determined experimentally.

When the purge valve is closed, the integration of the stack current is reset, as shown in Fig. 11. The maximum integrated current density used for simulations is $E_{crit} = 5000\ A\ s\ m^{-2}$ and the opening time is $t_{open} = 1$ s.

For different current modes, the controllers designed are switched based on the current amplitude requested. Performance of the control strategies in terms of tracking the pressure of supplied fuel and stabilizing SR_{H_2} of the FDS are analyzed along with rejection behavior for disturbances such as stack current and purging operations.

6. Analysis of simulation results of FDS with feed-back controllers

The FDS with designed controllers is implemented in the MATLAB/SIMULINK environment. Simulations are performed to study the pressure and SR responses when multiple steps of the stack current density are applied. Particularly, step responses of the designed

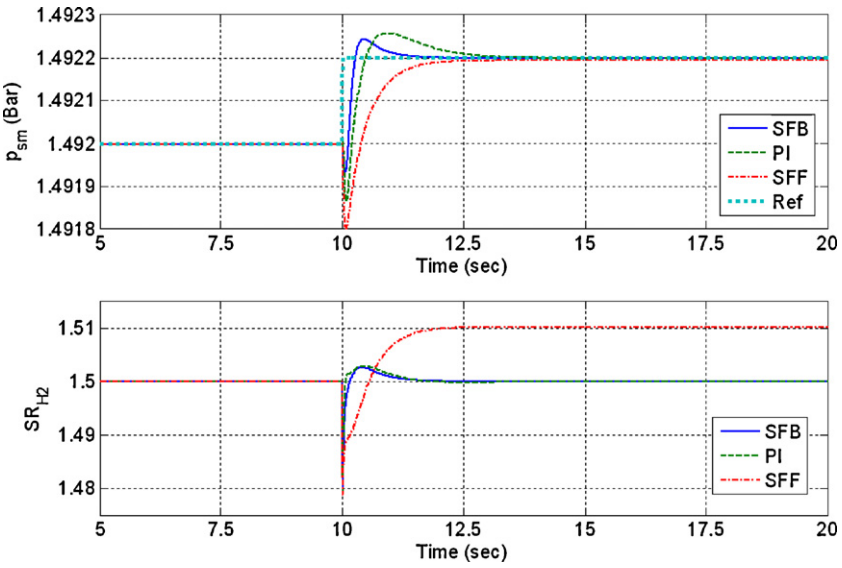

Fig. 12. Step response in medium current mode.

system for three different controllers are compared. The three controllers are the decentralized PI controller [4] (u_{fcv}–p_{sm} loop: $K_{P,p_{sm}} = 40$; $K_{I,p_{sm}} = 80$; and $u_{bl,n}$–SR_{H_2} loop: $K_{P,SR} = 3$, $K_{I,SR} = 6$), static feed forward controller (SFF), and the SFB controller for the medium and high current mode.

For the medium current mode, a step of the current density from 7000 to 7100 A m^{-2} is applied at 10th second and the responses of p_{sm} and SR_{H_2} are shown in Fig. 12, where the reference value of p_{sm} is calculated using Eq. (55).

Comparisons of step responses show that the p_{sm} using the SFB controller reaches the steady value at about 1 s with small overshoots, while the PI and SFF controllers take about 2.5 s to reach a steady state. On the other hand, the SR_{H_2} shown in Fig. 12 respond differently. The SFB and PI controllers enable the SR_{H_2} to return to 1.5 in about 1.2 s, while the SFF controller can reach a steady state, but with an error.

For high current mode, responses of p_{sm} and SR_{H_2} are shown in Fig. 13, where a step current from 9000 to 9100 A m^{-2} at 10th second is applied. The settle time of p_{sm} for the SFB and the PI controller are about 2.5 s and 3 s, respectively. For the response of SR_{H_2}, SFF cannot reach to the reference value, while the settle time using the SFB control is about 0.5 s that is smaller than that using the PI control.

In realty, the stack current and cathode pressure vary continuously in the three modes along with periodic purging operations. To mimic real operations, a multi-step stack current density is applied to the FDS with the fuel cell stack and at the same time a multi-step noise is added to the cathode pressure (p_{ca}) that is calculated by Eq. (55) as the dotted line in Fig. 14. This represents the reference pressure of the anode supply manifold. In addition, the purging valve is controlled by on-line calculations as shown in Fig. 14 depending on the variations of the stack current. The results show that the time interval between sequent purging operations gets shorter in the high current range, but larger in the low current range.

The initial values of the hydrogen partial pressures and angular velocity are given by the interpolation of curves of the steady state from the current density, while that of p_{em} for low current mode at the given multi-step current density is 1.4 bar. All initial values of water activities are set to be 10 to observe the purging effect on the liquid water.

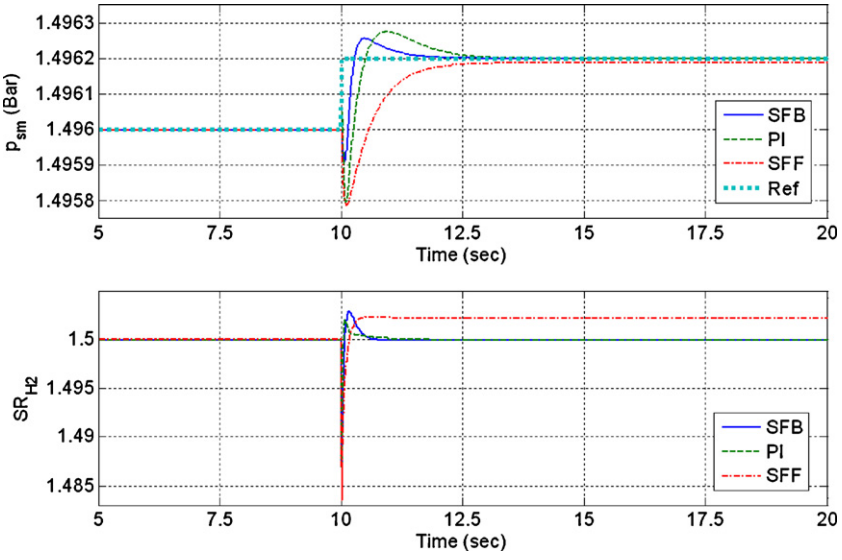

Fig. 13. Step response in high current mode.

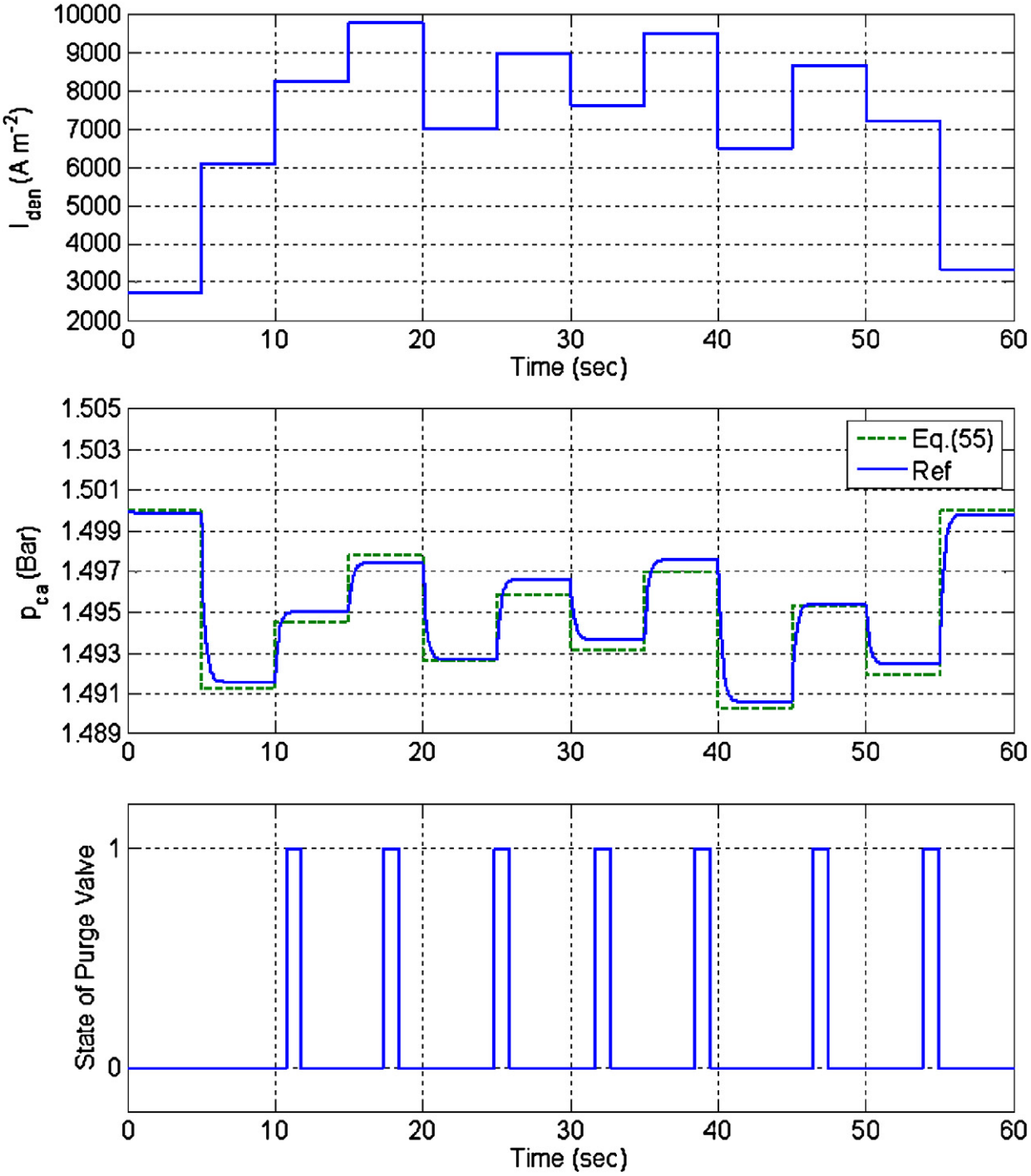

Fig. 14. Multi-step stack current, cathode pressure and purging operation.

The responses of p_{sm} under the change of stack current and purging operating for the three controllers are shown in Fig. 15, where the PI gains are the same as those in the previous case. When the load current is low, the PI gain for SR_{H_2} control are the same as that used in the SFB control for the SISO system. Thus, the p_{sm} at the beginning and end of the stack current curve is stabilized by the low-pressure regulator as shown in Fig. 14. When the load current changes between the medium and high modes, the two controllers and observers are automatically switched. The actual value of the pressure, p_{sm}, tracks the reference curve by the controllers. The settle time of the SFB control is the smallest, while the overshoot of the PI control is the largest among the three controllers. The step response of the SFF shows that the control cannot follow the reference value of the supply manifold pressure at steady state. At purging, it takes about 1 s for the SFF control to reach the steady state, but with a constant error, while SFB and PI controls are able to reach the reference value as shown in Fig. 14, while purging is operating at the 17th second. The settle time of the SFB control is about 0.7 s after the start of the purge valve, and 0.3 s after the shutdown of the purge valve, while a longer settle time of the PI control is observed, as shown in Fig. 14.

With respect to response of SR_{H_2} shown in Fig. 16, where performances of three controllers are different, the SFF control has the largest steady state error and overshoot among others. The set-

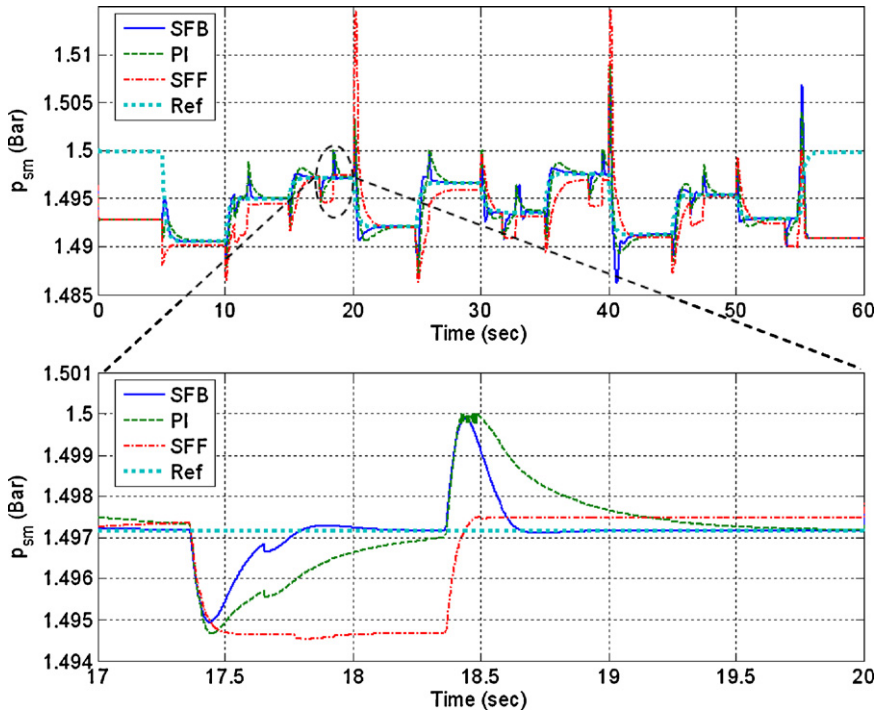

Fig. 15. Response of anode supply manifold pressure under three different controllers at a multi-step stack current under purging operation.

tle time of the SFB and PI controls are comparable, but the SFB control has a slightly higher overshoot than the PI control, while the SFB control converges more rapidly to the reference, especially when purging is in operation as shown in Fig. 16. The SFB control allows for stabilizing the SR_{H_2} to a reference within about 0.3 s after purging, while it takes about 1 s for the PI control to reach the reference.

As shown in Fig. 17, water activities in the supply manifold rapidly drop to about 1 at the first purging for three controllers. Then, the water activities change in the range of 1–2 periodically with the purging process when the SFB and PI control are applied. In contrast, the SFF control shows a highest peak value of the water activity for the SFF control after the first purging. As a result, the amount of liquid water in the supply manifold is very small under the current purging strategy at the normal working conditions of a fuel cell stack. It should be noted that the water activity in the supply manifold frequently becomes less than 1 during purging, which affects the estimation of the SR_{H_2} as shown in Eq. (60), where

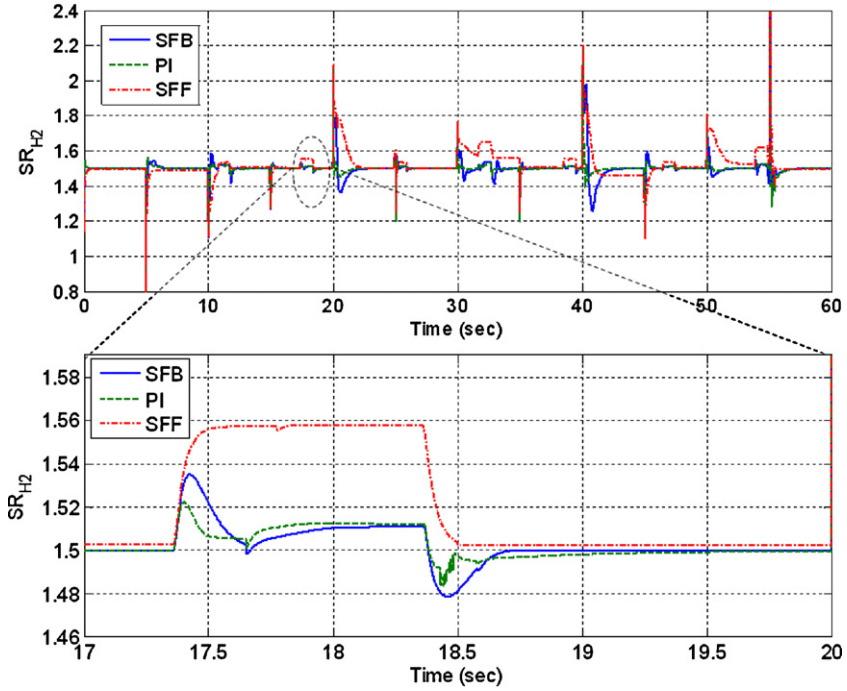

Fig. 16. Response of stoichiometric ratio under the three controllers, at a multi-step stack current under the purging operation.

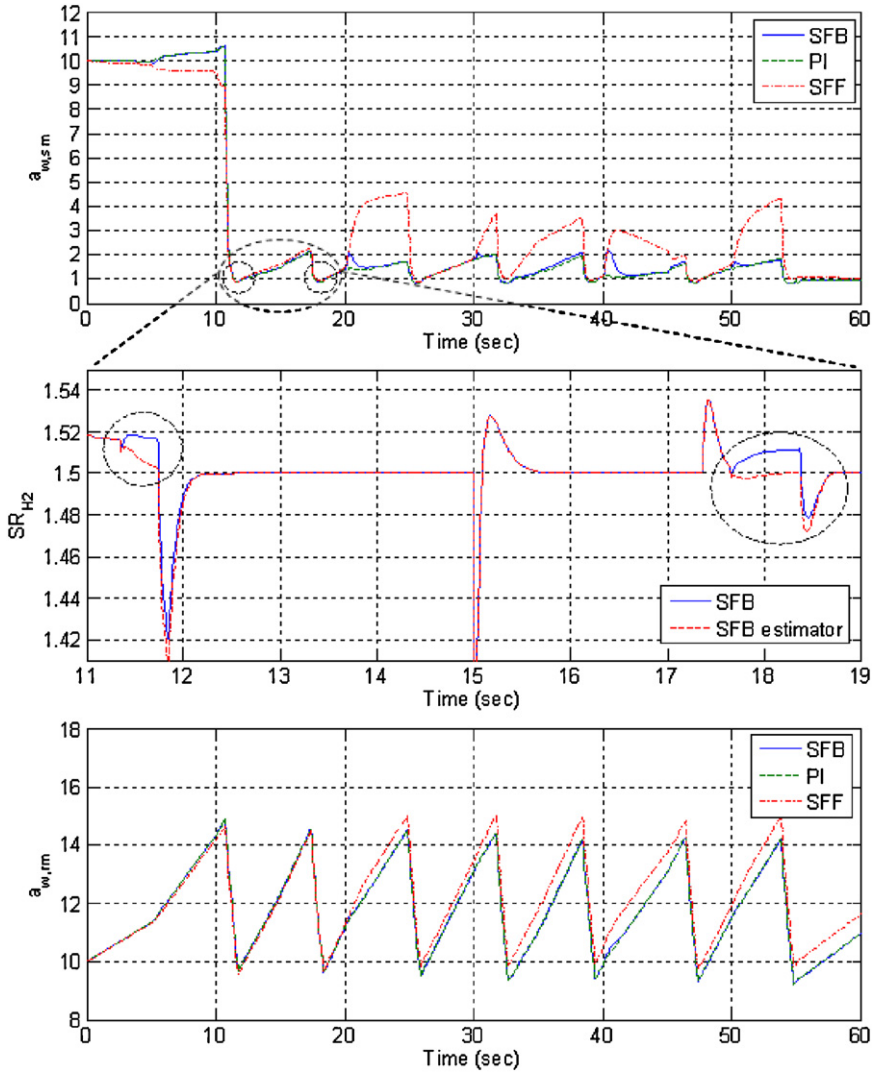

Fig. 17. Response of water activity in manifolds at a multi-step stack current.

the supply manifold water activity is assumed to be greater than 1. The error of the estimation is shown in Fig. 17, where the estimated SR_{H_2} gets lower than the real value when purging. The water activity in the return manifold varies like a triangle wave as plotted in Fig. 17, where the range of water activity varies from 9 to 15. The peak values of the water activities in the supply manifold decrease with time. Thus, the liquid water amount in the return manifold is larger than that in supply manifold, and purging can restrict and reduce the amount of liquid water under the current purging control strategy.

As shown in Fig. 18, the water activities in the GFC decreases to 1 in about 40 s because of the purging that decreases the water activity in the GFC in the first 40 s. However, the purging does not directly affect the water activity in the GDL. After the water activity of the GFC has reached to 1, the water activity in the GDL drops from 10 to 1 in about 12 s. In the last seconds, the water activities in the GFCs and GDL becomes near the constant 1, which indicates that a small amount of liquid water may appear in the anode of the fuel cell under the normal working conditions of current variations and purging.

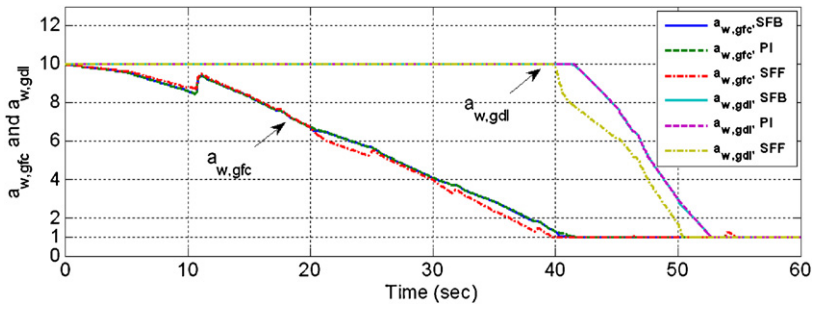

Fig. 18. Response of water activity in fuel cells at a multi-step stack current.

From the analysis above, it can be concluded that the SFF control always causes steady state error and produces the largest amount of liquid water accumulated in the supply and return manifolds. In contrast, the SFB control allows following the pressure in the anode supply manifold to that in the cathode pressure with the shortest rise time and the smallest overshoot compared to others. In addition, SR_{H_2} is well maintained at the reference value with a shortest settle time and an acceptable overshoot when a multi-step current is applied with periodic purging. Since the track performance of cathode pressure is more important than the maintenance of SR_{H_2}, the SFB control outperforms the other controls with respect to rejection of the disturbances.

7. Conclusion

In this paper, we developed a control-oriented model of a FDS that includes two supply lines and two recirculation loops. The FDS model is then connected to a dynamic model for half a cell on the anode side that considered the liquid water effect in GFC, GDL and CL.

Based on the integrated model above, a control strategy is proposed, which consists of a PI controller for low current mode and a new state feedback controller with an observer for medium and high current mode in addition to purging controls. The SFB is compared with two classic controllers and its performance is analyzed. The major findings of this study are summarized as follows:

[1] The FDS with the control strategy proposed can dynamically follow references of flow rate and pressure of fuel supply at different load conditions. The FDS with the controller is likely to be instable without purging because of transport of water from the cathode to the anode, and consequent condensation of vapor in the manifolds.

[2] Evaluations of three control strategies indicates that the SFB control with integral and observer shows the best performance with respect to tracking capability for cathode pressure and disturbance rejection.

[3] Analysis shows that the water activities in GFC and GDL are regulated at about constant 1 for the dynamic purging control dependent on the current load change, which prevents the water flooding at anode side and in the supply and return manifolds.

Future work will include effects of temperature changes in manifolds and fuel cells and automatic tuning of parameters dependent upon the load current using advanced controls.

References

[1] J.T. Pukrushpan, H. Peng, A.G. Stefanopoulou, J. Dyn. Syst. Meas. Contr. 126 (2004) 14–25.
[2] C. Bao, M. Ouyang, B. Yi, Int. J. Hydrogen Energy 31 (2006) 1879–1896.
[3] A.Y. Karnik, J.H. Buckland, J. Sun, 2007 American Control Conference, New York City, USA, 2007.
[4] J. He, S.-Y. Choe, C.-O. Hong, J. Power Sources 185 (2008) 973–984.
[5] F. Marsano, L. Magistri, A.F. Massardo, J. Power Sources 129 (2004) 216–228.
[6] A.Y. Karnik, J. Sun, J.H. Buckland, 2006 American Control Conference, Minneapolis, MN, USA, 2006.
[7] Y. Zhu, Y. Li, J. Power Sources 191 (2009) 510–519.
[8] J.P. Jensen, A.F. Kristensen, S.C. Sorenson, N. Houbak, E. Hendricks, in: SAE 910070.
[9] P. Moraal, I. Kolmanovsky, International Congress and Exposition, Detroit, MI, 1999.
[10] C.R. Wilke, J. Chem. Phys. 18 (1950) 517–519.
[11] A.Z. Weber, J. Newman, Chem. Rev. 104 (2004) 4679–4726.
[12] A.Z. Weber, J. Newman, J. Electrochem. Soc. 151 (2004) A325–A331.
[13] T.E. Springer, T.A. Zawodzinski, S. Gottesfeld, J. Electrochem. Soc. 138 (1991) 2334–2342.
[14] J.T. Hinatsu, M. Mizuhata, H. Takenaka, J. Electrochem. Soc. 141 (1994) 1493–1498.
[15] S. Ge, X. Li, B. Yi, I.-M. Hsing, J. Electrochem. Soc. 152 (2005) A1149–A1157.
[16] S. Motupally, A.J. Becker, J.W. Weidner, J. Electrochem. Soc. 147 (2000) 3171–3177.
[17] A. Mokmeli, S. Asghari, Int. J. Hydrogen Energy (2010), doi:10.1016/j.ijhydene.2010.1003.1079.